



Technical Note

# A Machine Learning-Based Multiple Cloud Vertical Structure Parameter Prediction Algorithm Only Using OCO-2 Oxygen A-Band Measurements

Yixiao Lei <sup>1</sup> , Siwei Li <sup>1,2</sup> and Jie Yang <sup>1,2,\*</sup>

<sup>1</sup> Hubei Key Laboratory of Quantitative Remote Sensing of Land and Atmosphere, School of Remote Sensing and Information Engineering, Wuhan University, Wuhan 430079, China

<sup>2</sup> Hubei LuoJia Laboratory, Wuhan University, Wuhan 430079, China

\* Correspondence: jie.yang@whu.edu.cn

**Abstract:** Measurements of the global cloud vertical structure (CVS) are critical to better understanding the effects of the CVS on climate. Current CVS algorithms based on OCO-2 have to be combined with cloud top height products from CALIPSO and CloudSat, which are no longer available after these two satellites left A-Train in 2018. In this paper, we derive a machine learning-based algorithm using only OCO-2 oxygen A-band hyperspectral measurements to simultaneously predict the cloud optical depth (COD), cloud top pressure (p<sub>top</sub>), and cloud pressure thickness (CPT) of single-layer liquid clouds. For validation of real observations, the root mean square errors (RMSEs) of the COD, p<sub>top</sub>, and CPT are 7.31 (versus the MYD06\_L2), 35.06 hPa, and 26.66 hPa (versus the 2B-CLDCLASS-LIDAR). The new algorithm can also predict CVS parameters trained with p<sub>tops</sub> from CALIPSO/CloudSat or CODs from MODIS. Controlled experiments show that known p<sub>tops</sub> are more conducive to CPT prediction than known CODs, and experiments with both known CODs and p<sub>tops</sub> obtain the best accuracy of RMSE = 20.82 hPa. Moreover, a comparison with OCO2CLD-LIDAR-AUX products that rely on CALIPSO shows that our CVS predictions only using OCO-2 measurements have better CODs for all clouds, better p<sub>tops</sub> for clouds with a p<sub>top</sub> < 900 hPa, and better CPTs for clouds with a CPT > 30 hPa.

**Keywords:** OCO-2; oxygen A-band; cloud vertical structure; machine learning



**Citation:** Lei, Y.; Li, S.; Yang, J. A Machine Learning-Based Multiple Cloud Vertical Structure Parameter Prediction Algorithm Only Using OCO-2 Oxygen A-Band Measurements. *Remote Sens.* **2023**, *15*, 3142. <https://doi.org/10.3390/rs15123142>

Academic Editors: Alexander Kokhanovsky, Luca Lelli and Daniel Rosenfeld

Received: 16 May 2023  
Revised: 13 June 2023  
Accepted: 13 June 2023  
Published: 16 June 2023



**Copyright:** © 2023 by the authors. Licensee MDPI, Basel, Switzerland. This article is an open access article distributed under the terms and conditions of the Creative Commons Attribution (CC BY) license (<https://creativecommons.org/licenses/by/4.0/>).

## 1. Introduction

Clouds are an essential component of the atmosphere, covering about two-thirds of the Earth [1] and playing a significant role in the hydrological cycle and radiation budget [2–4]. Clouds affect the Earth's climate by interacting with long- and short-wave radiation, resulting in heating and cooling effects [5–8]. The uncertainties of cloud effects are greatly related to the lack of cloud vertical structure (CVS) information, which has an impact on microphysical processes in clouds and, thus, on precipitation intensity [9,10]. Furthermore, changes in the CVS affect the distribution of radiative heating/cooling and latent heating rates, affecting atmospheric circulations [11,12]. As the water cycle and cloud radiative effects are largely affected by the CVS, it is important to measure and collect CVS information to analyze its influence on climate.

On 28 April 2006, the National Aeronautics and Space Administration (NASA) launched CloudSat and Cloud–Aerosol Lidar and Infrared Pathfinder Satellite Observation (CALIPSO) as part of the Afternoon Constellation (A-Train), which makes CVS observation available [13,14]. The Cloud Profiling Radar (CPR) onboard CloudSat, and the Cloud–Aerosol Lidar with Orthogonal Polarization (CALIOP) onboard CALIPSO, are two important active sensors that can provide CVS products [15]. However, there are few satellites with active sensors, and active sensors have a narrow swath.

Several passive remote sensing studies investigated the feasibility of retrieving the cloud top height (CTH) by estimating the photon path length through the atmosphere from the absorption of the water vapor absorption band, CO<sub>2</sub> absorption band, or oxygen A-band [16,17]. The oxygen A-band is an absorption band at a wavelength near 760 nm, which does not overlap with other absorption bands, contains strong absorption lines, and the mixing ratio of the oxygen is fixed [18]. Since the 1960s, researchers have begun to develop algorithms based on oxygen A-band measurements to retrieve more CVS properties, including cloud geometric thickness (CGT), due to the improvement in the spectral resolution of oxygen A-band observations.

Some CPT retrievals were proposed based on single-angle moderate spectral resolution (about 0.3 nm) oxygen A-band measurements [19], but further studies revealed that such measurements contain only two independent pieces of information, i.e., the cloud optical depth (COD) and  $p_{top}$ , and the CPT retrieval was inadequate [20]. To obtain reliable CPTs, researchers introduced  $p_{top}$  products of other payloads [21,22], used multi-angular measurements of the oxygen A-band [23,24], or combined oxygen A-band and B-band measurements [25].

Other studies focused on the hyperspectral oxygen A-band measurement, which contains more CVS information, including the COD,  $p_{top}$ , and CPT [19,26–29], such as the observations from the OCO-2 (Orbiting Carbon Observatory-2). The OCO-2 was launched in 2014, and the onboard spectrometer has a hyperspectral resolution of 0.04 nm in the oxygen A-band [30–33]. Based on the OCO-2 oxygen A-band measurements and the constraint of the  $p_{tops}$  from CALIPSO, Richardson et al. (2019) retrieved the COD,  $p_{top}$ , and CPT and released the OCO2CLD-LIDAR-AUX dataset. Yang et al. (2021) proposed a semi-analytical algorithm for fast CPT retrievals using OCO-2 oxygen A-band measurements and collocated  $p_{tops}$  and CODs from the A-train satellites. In short, the  $p_{top}$  from CloudSat/CALIPSO is an indispensable input in current algorithms.

However, CloudSat exited the A-Train orbit due to the loss of one of its reaction wheels, and CALIPSO exited the A-Train for simultaneous measurements following CloudSat (<https://atrain.nasa.gov/atrainats.php>, accessed on 13 May 2023). As a result, the above CPT retrieval algorithm based on the OCO-2 is no longer available due to the lack of collocated  $p_{top}$  data. It is urgent to develop a new CVS prediction algorithm only using OCO-2 oxygen A-band measurements.

In this paper, we present a fast CVS prediction algorithm for single-layer liquid clouds based on a neural network (NN) using OCO-2 oxygen A-band measurements. Our algorithm, in contrast to earlier algorithms, can simultaneously predict the three CVS parameters of the COD,  $p_{top}$ , and CPT without using the collocated  $p_{top}$  data. Instead, it only requires the inputs of OCO-2 oxygen A-band measurements, the surface pressure, and the solar zenith angle, which provides the possibility for future cloud geometrical thickness prediction to get rid of the limitation of joint observation. Compared with previous optimal estimation-based algorithms developed by Richardson et al. [26] and Yang et al. [31], our algorithm can predict CPT without collocated  $p_{tops}$  and has better accuracy than these optimal estimation-based algorithms.

This paper is organized as follows: Section 2 describes the data, Section 3 describes the methodology, Section 4 presents the CVS results and their evaluations, and Section 5 provides the conclusions.

## 2. Data

### 2.1. OCO-2

The OCO-2 leads the A-Train, crosses the equator at approximately 13:30 local time, and has a revisiting time of 16 days [34]. It has two operational viewing modes, the nadir mode and the glint mode [35]. The OCO-2 carries the spectrometer, the OCO, and its observations consist of eight footprints with a resolution of approximately 1.29 km × 2.25 km in nadir mode. The OCO-2 mission is to retrieve the atmospheric CO<sub>2</sub> concentration (XCO<sub>2</sub>) using reflected sunlight [36,37], where oxygen A-band measurements can provide

constraints on the surface pressure and reduce uncertainties due to cloud and aerosol scatterings [38]. In this paper, the OCO-2 oxygen A-band measurements are further used to predict the CVS.

The OCO-2's product, the OCO-2 L1bSc (version 8r), records a bad-sample list, solar zenith angle, viewing geometry, and radiance observation. The bad-sample list is used to remove useless channels in radiance observation to avoid the impact of damaged pixels on CVS prediction. At present, Richardson et al. released the OCO2CLD-LIDAR-AUX product based on OCO-2 radiance observation and collocated the constraints of the CTH from CALIPSO [26], but this product is no longer available after the exit of CALIPSO from the A-Train.

## 2.2. CALIPSO and CloudSat

CALIPSO and CloudSat follow behind the OCO-2 by approximately 7.5 and 9 min in the A-Train so that their footprints can be collocated with the closest nadir footprint of the OCO-2. The CPR on CloudSat and the CALIOP on CALIPSO are both active sensors. The CPR can detect the cloud base height of thick clouds with a vertical resolution of 500 m, while the CALIOP can measure the CTH with a higher vertical resolution of 60 m [39]. The 2B-CLDCLASS-LIDAR (version P1\_R05) product combines the strengths of CPR and the CALIOP and provides better CVS properties [39], including cloud top and base heights, the number of cloud layers, and the cloud phase and its confidence level.

Furthermore, the CloudSat product, 2B-CLDCLASS (version P1\_R05), including precipitation [40], and the CALIPSO product, CAL\_LID\_L2\_05kmA-Lay (version 4.20), including aerosol, are used to select candidate cloudy scenes.

## 2.3. MODIS

The passive sensor, the Moderate Resolution Imaging Spectroradiometer (MODIS), carried by Aqua, has 36 spectral channels from the visible to the infrared and a spatial resolution of 1 km at nadir [41]. The Aqua MYD06\_L2 product (collection 6.1) records the cloud mask, cloud optical depth, and thermodynamic phase [42]. Continuous spatial coverage of the MODIS is used to find clouds with similar properties covering the triad of OCO, CALIOP, and CPR footprints, providing references for the combination of multi-source A-Train satellites [43].

## 2.4. Auxiliary Data

The input surface pressure and the height-pressure mapping table for converting the cloud top and base height to pressure are provided by the European Center for Medium-Range Weather Forecasts (ECMWF).

# 3. Method

## 3.1. Data Collocation

OCO-2 measurements are used to predict the CVS, while products from the MODIS, CALIPSO, and CloudSat are collocated with OCO-2 observation for training, validation, and controlled experiments. The collocation can be divided into two steps, following Yang et al. (2021).

Step 1: Find candidate scenes. For each OCO footprint, find the nearest CPR and CALIOP footprints within a center distance of 15 km and the three closest MODIS footprints around the OCO, CPR, and CALIOP footprints. Only OCO footprints in nadir mode are used because of the search distance limitation. The three MODIS footprints are required to be cloudy scenes with a valid COD value. The six footprints above are considered a candidate collocated scene. A boundary rectangle surrounding these six footprints is used to calculate the COD by averaging all valid COD values in the rectangle.

Step 2: Select single-layer liquid clouds. A filter is used to ensure that the footprints in a candidate scene have similar cloud properties. Products from six footprints are used

in the filter to exclude no-liquid, multi-layer clouds and clouds with above aerosol or precipitation. Detailed criteria of the filter are listed in Table 1.

**Table 1.** The filter for candidate scenes.

Number	Measurements or Products	Criterion
1	MYD06_L2	Confidently or probably cloudy
2	MYD06_L2	Existing values for cloud optical depth
3	MYD06_L2 and 2B-CLDCLASS-LIDAR	All liquid phase, CPR confidence level > 4
4	2B-CLDCLASS-LIDAR	Single-layer cloud
5	2B-CLDCLASS	No precipitation
6	CAL_LID_L2_05kmALay	No above-cloud aerosol

The difference between our filter and Yang's is that we take into account cloudy scenes over both land and ocean and do not remove cases where the cloud optical depth is less than 5 or more than 50.

OCO-2 measurements in 2016 are collocated with products from A-Train satellites, with 3,648,796 cases selected in total after filtering. Each selected case has six fields, including the COD from the Aqua MYD06\_L2 product, the cloud top pressure ( $p_{top}$ ), and the cloud pressure thickness (CPT), converted from 2B-CLDCLASS-LIDAR, oxygen A-band radiance, and the solar zenith angle from the OCO-2 L1bSc product and the surface pressure from ECMWF.

### 3.2. Data Preprocessing

Damaged channels and the channels containing strong solar absorption features are removed to prevent interference with CVS information in oxygen A-band observations, following the work of Lee et al. [33]. The wavelength of channels varies slightly between eight footprints, which means the channels affected by solar lines are not completely identical for different footprints. Therefore, channels affected by the solar line for each footprint are separately removed and intersected to obtain the remaining channels, leaving a total of 725 channels.

Datasets are divided into training, validation, and test datasets by longitude, avoiding sample leakage and overfitting when all sets contain similar neighboring samples. Samples with OCO-2 pixels located at 65–50°W and 0–15°E belong to the test dataset, samples with OCO-2 pixels located at 45–60°E belong to the validation dataset, and the remaining samples belong to the training dataset. The training dataset, test dataset, and validation dataset contain 2,979,059, 467,314, and 202,423 samples, respectively.

The distribution histograms of the COD,  $p_{top}$ , and CPT in the training, test, and validation datasets are shown in Figure 1. Although the three datasets cover different regions, they follow similar sample distributions, which is important for successfully training the machine learning model. Samples with a CPT < 30 hPa show regular jumps, which is attributed to the limitation of the vertical resolution of the CALIOP [39].

### 3.3. Neural Network Design

Artificial neural networks consist of interconnected processing units and usually contain an input layer, an output layer, and multiple hidden layers. The individual computational units in each layer are called neurons. The back-propagation neural network (BPNN) is a multi-layer NN based on the back-propagation algorithm. With forward propagation of information and backward propagation of error, information is transmitted between layers in the training process. A loss function, quantifying the model errors, is minimized with the backward propagation iteration until certain stopping conditions are met. NNs are widely used in atmospheric parameter retrievals and show great performance [44–48]. NNs trained with the 2B-CLDCLASS-LIDAR product inherit the uncertainties of the product rather than the uncertainties of homogeneous cloud assumptions in the radiative transfer model based

on the oxygen A-band, which proved to be significant to the retrieval error in Yang et al.'s work [31], and the NN model can learn some statistical relationships between the input and output.

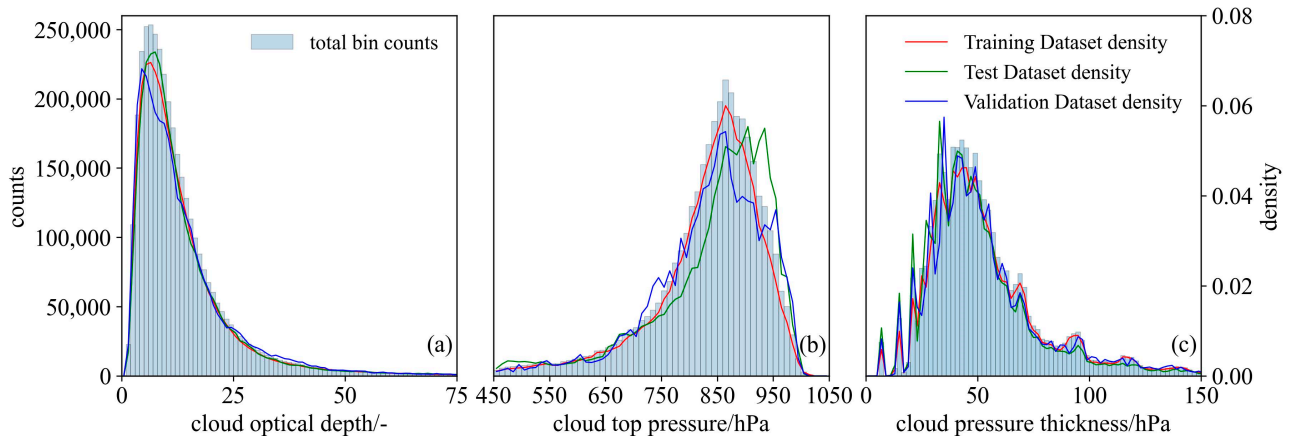


**Figure 1.** Histograms of the cloud vertical structure in the training, test, and validation datasets: (a) cloud optical depth, bin size = 1; (b) cloud top pressure, bin size = 6 hPa; (c) cloud pressure thickness, bin size = 2 hPa.

Input and output data for model training are listed in Table 2. Both inputs and outputs are standardized to unify different dimensions. In this study, the mean squared error is used as the loss function, and the rectified linear unit (ReLU) is used as the activation function. We also use the “Adam” solver and dropout with an eliminated fraction of 10%. The validation dataset and early stop method are used to prevent overfitting.

**Table 2.** All fields of collocation datasets, sources of fields, and whether they are input or output for the model.

Fields	Source	Input/Output
Cloud optical depth	MYD06_L2	output
Cloud top pressure	2B-CLDCLASS-LIDAR	output
Cloud pressure thickness	2B-CLDCLASS-LIDAR	output
Surface pressure	ECMWF	input
Solar zenith angle	OCO-2 L1bSc	input
OCO-2 oxygen A-band radiance	OCO-2 L1bSc	input

Three NN models with different layers or nodes are tested to determine suitable network settings for CVS retrievals. Table 3 lists the settings and accuracy for each candidate model. The 2-layer model with 300 nodes and the 3-layer model with 200 nodes do not significantly improve the accuracy, but they bring more computational costs, and the RMSE of the 2-layer model with 100 neurons and the 1-layer model with 200 neurons increases. Therefore, the 2-layer model with 200 nodes is constructed for CVS prediction under consideration of accuracy and training costs.

**Table 3.** Three NN models with different settings and their prediction accuracy.

Net Settings		Accuracy (Root Mean Square Error)		
Hidden Layers	Nodes in Each Layer	COD	p_top	CPT
2	200	7.31	35.06 hPa	26.66 hPa
2	300	7.35	33.88 hPa	26.48 hPa
3	200	7.48	34.48 hPa	26.80 hPa
2	100	7.36	36.84 hPa	26.75 hPa
1	200	7.46	39.37 hPa	26.84 hPa

## 4. Results

### 4.1. CVS Predictions

The performance of the machine learning-based CVS prediction algorithm is evaluated by comparing the results of the test dataset with the COD from the MYD06\_L2 product and the  $p_{top}$  and CPT from the 2B-CLDCLASS-LIDAR product.

Figure 2 shows the prediction accuracy. The correlation coefficients ( $R$ ) of the COD,  $p_{top}$ , and CPT are, respectively, 0.8178, 0.9514, and 0.5280, and the root mean square errors (RMSEs) are, respectively, 7.31, 35.06 hPa, and 26.66 hPa. The predicted CODs and  $p_{top}$ s are distributed along the 1:1 line with a higher correlation coefficient and lower mean absolute relative errors (32.22% for the COD and 2.89% for the  $p_{top}$ ) compared to the CPT results (42.98%). In Figure 2c, there are stripes around the predicted CPTs of geometrically thin clouds (CPT < 20 hPa), which is probably affected by the vertical resolution of the CALIOP. With a vertical resolution of 60 m [39], the geometrical thickness of thin clouds falls into specific values. In the lower atmosphere, 60 m is about 6 hPa, which coincides with the spacing between the stripes in Figure 2c. These stripes are also one of the main reasons for the large prediction error of thin clouds.

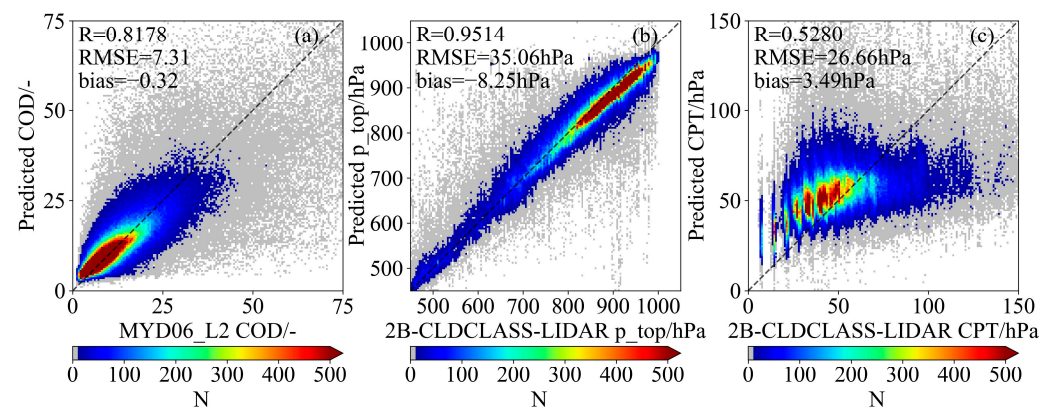


**Figure 2.** Prediction result based on the test dataset. (a) COD, bin size =  $0.5 \times 0.5$ ; (b)  $p_{top}$ , bin size =  $4 \text{ hPa} \times 4 \text{ hPa}$ ; (c) CPT, bin size =  $1 \text{ hPa} \times 1 \text{ hPa}$ . Bins with counts less than 10 are shown in gray.

The algorithm is also verified with samples randomly split, and prediction accuracies are listed in Table S1. Furthermore, a test on cases with above-cloud aerosols is conducted and displayed in Figure S1, and a cloud profile showing the tops and bottoms of the predicted CVS by Model I along the OCO-2 track is presented in Figure S2.

Figure 3a–c present the variations of the predicted CVS's RMSE. For CODs lower than 75, the RMSE increases approximately linearly from about 3 to about 30 in Figure 3a. The RMSE of the  $p_{top}$  decreases from about 50 hPa at  $p_{top} = 650$  hPa to about 23 hPa at  $p_{top} = 880$  hPa and then rises to 50 hPa in Figure 3b. The best accuracy of the  $p_{top}$  near 880 hPa benefits from large samples, as shown in Figure 3e, and worse for small samples from 450 hPa to 650 hPa. Small samples also lead to the fluctuating RMSE of the  $p_{top}$ . In Figure 3c, the RMSE of the CPT gradually decreases from about 45 hPa at CPT = 6 hPa to about 12 hPa at CPT = 55 hPa and then rises to about 80 hPa. The effect of sample size on the RMSE of the CPT is evident in cases where the CPT is less than 40 hPa, and the RMSEs on the strips (7 hPa, 14 hPa, and so on) are always local minimums. Several factors exacerbate the RMSE of the CPT in geometrically thin cloud scenes (CPT < 40 hPa), including the limitation of the CALIOP's vertical resolution on the reference CPT's accuracy, the ignored small samples in the model training, and the difficulty of distinguishing between low oxygen absorption inside geometrically thin clouds and high oxygen absorption over clouds.

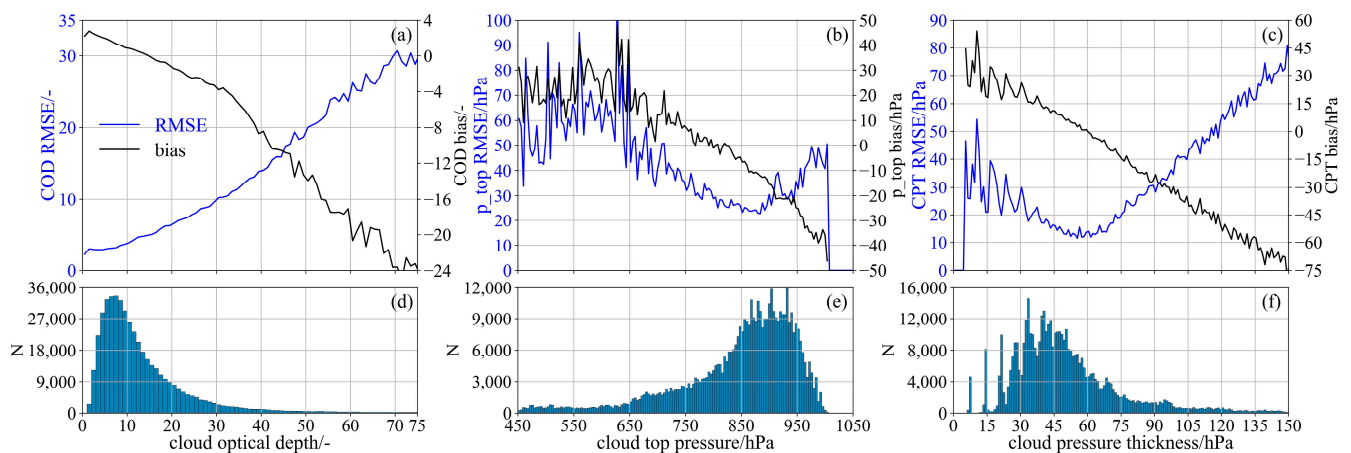


**Figure 3.** RMSEs and biases of prediction results based on the test dataset. (a–c) display the RMSE and bias of (a) COD, bin size = 0.5, (b)  $p_{top}$ , bin size = 4 hPa, and (c) CPT, bin size = 1 hPa. (d–f) display the distribution of COD,  $p_{top}$ , and CPT.

In Figure 3a–c, the average errors (bias) of the predicted COD,  $p_{top}$ , and CPT vary similarly, turning from overestimation to underestimation around their average values (13.86 for the COD, 843.49 hPa for the  $p_{top}$ , and 52.39 hPa for the CPT). Model uncertainties may be the main reason because NN predictions tend to make predictions with higher probabilities, so the prediction results tend to be distributed in the parts of the target distribution with the most samples.

In summary, the NN model only using the OCO-2 hyperspectral oxygen A-band observation can predict three CVS parameters, i.e., the COD,  $p_{top}$ , and CPT. Among them, the prediction uncertainty of the CPT is the largest but still better than the algorithm of Yang et al. (2021, RMSE = 38.5 hPa), which also requires inputs of COD from the MODIS and  $p_{top}$  from CloudSat/CALIPSO.

#### 4.2. Influence of COD and $p_{top}$ on CPT Prediction

However, known CODs and  $p_{tops}$  still contribute to the prediction of the CPT and can be added to our algorithm. Table 4 shows four controlled experiments. Model I is introduced in Section 4.1 and is used as a baseline for comparison. Model II, III, and IV are trained with the same neural network structure as Model I but vary when either the COD and/or  $p_{top}$  are used as the input instead of as the output.

**Table 4.** Four prediction experiments designed for analyzing the contribution of known CODs and  $p_{tops}$  to CPT retrievals. In Model II, COD is used for input, and only  $p_{top}$  and CPT are the target outputs. In Model III,  $p_{top}$  is used for input, and only COD and CPT are the target outputs. In Model IV, COD and  $p_{top}$  are used for input, and only CPT is the target output.

Experiment	COD	$p_{top}$	CPT
Model I	Output	Output	Output
Model II	Input	Output	Output
Model III	Output	Input	Output
Model IV	Input	Input	Output

##### 4.2.1. Prediction Improvement with Different Inputs

Figure 4 shows the CPT results of Model I–IV. With known CODs or  $p_{tops}$ , Model II–IV enhance the accuracy of the CPT compared with Model I, and more samples are closer to the 1:1 line. The R, RMSE, and bias of Model I–IV are listed in Figure 4. With known CODs (Model II), the R of the predicted CPT increases to 0.5840, and the RMSE and bias decrease to 25.42 hPa and 2.86 hPa. The COD provides information about in-cloud scattering. With known  $p_{tops}$  (Model III), the R of the predicted CPT increases more than

Model II, reaching 0.7225, and the RMSE and bias decrease more to 21.59 hPa and 0.36 hPa. The  $p_{top}$  plays a more significant role in CPT prediction than for the COD because the  $p_{top}$  impacts the oxygen absorption much more than the COD, which leads to a stronger constraint on CPT retrieval. When the  $p_{top}$  is known in the prediction, the accuracy of the predicted CPT can be significantly improved.

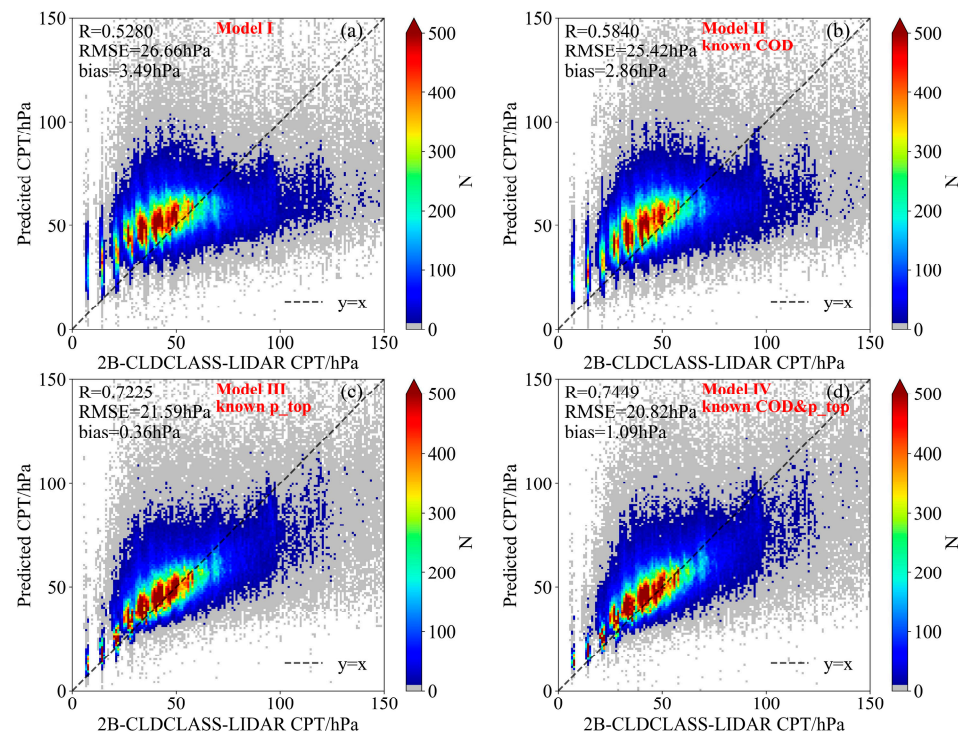


**Figure 4.** CPT prediction results with different input parameters versus 2B-CLDCLASS-LIDAR. (a–d), respectively, show the performance of Models I–IV. The bin size is 1 hPa  $\times$  1 hPa, and bins with counts less than 10 are shown in gray.

With known CODs and  $p_{tops}$  (Model IV), the R of the predicted CPT increases to 0.7449, and the RMSE and bias decrease to 20.82 hPa and 1.09 hPa. Compared with the previous fast CPT prediction algorithm, which required collocated CODs and  $p_{tops}$  [31], the NN model inherits the uncertainties of the 2B-CLDCLASS-LIDAR rather than the uncertainties of the assumptions in the radiative transfer model for CPT retrieval. Therefore, Model IV provides much more accurate CPT prediction results.

#### 4.2.2. Prediction Error with Different Input Variables

Figure 5 shows the variations of the CVS's RMSE in Model I–IV, which are used to analyze the influence of known CODs and  $p_{tops}$  of CPT prediction. The comparison of Models I and III in Figure 5a shows that the extra input of the  $p_{top}$  does not improve the RMSE of the COD remarkably. Meanwhile, the extra input of the COD does not improve the RMSE of the  $p_{top}$  in Figure 5b, suggesting that the COD and  $p_{top}$  are two pieces of independent information contained in OCO-2 oxygen A-band radiance.

Figure 5c compares the effects of known CODs or  $p_{tops}$  of the CPT results in the four experiments. The RMSE of Model II is slightly better than that of Model I, indicating that the COD input can provide a small amount of information for the CPT. This information is a bit more useful for the prediction of geometrically thin clouds (CPT < 30 hPa), whose RMSE is better improved. For geometrically thin clouds, it is difficult to effectively distinguish the absorption caused by single scattering in the cloud and absorption above the cloud. Known COD inputs can help determine the single scattering and multiple scattering in the cloud and then estimate oxygen absorption in the cloud and help CPT prediction.

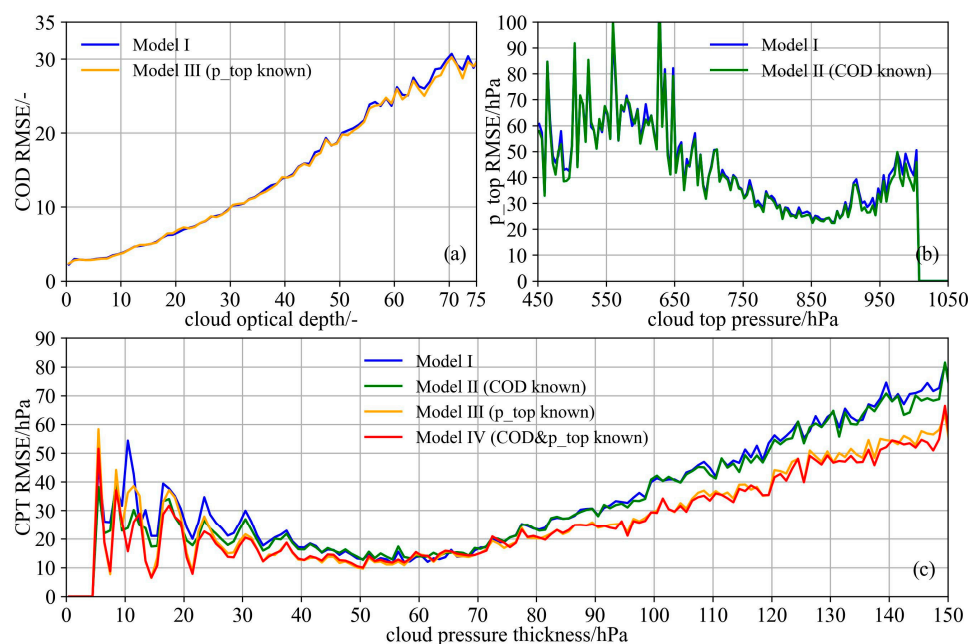


**Figure 5.** RMSEs of (a) COD, (b)  $p_{top}$ , and (c) CPT in Models I–IV.

Compared with Model II, the RMSE of Model III decreases significantly for all clouds, especially when the CPT > 80 hPa, proving that  $p_{top}$ s provide much more information than CODs for CPT predictions. The  $p_{top}$  input can provide oxygen absorption information above the clouds to help CPT prediction, no matter how geometrically thin or thick the cloud is.

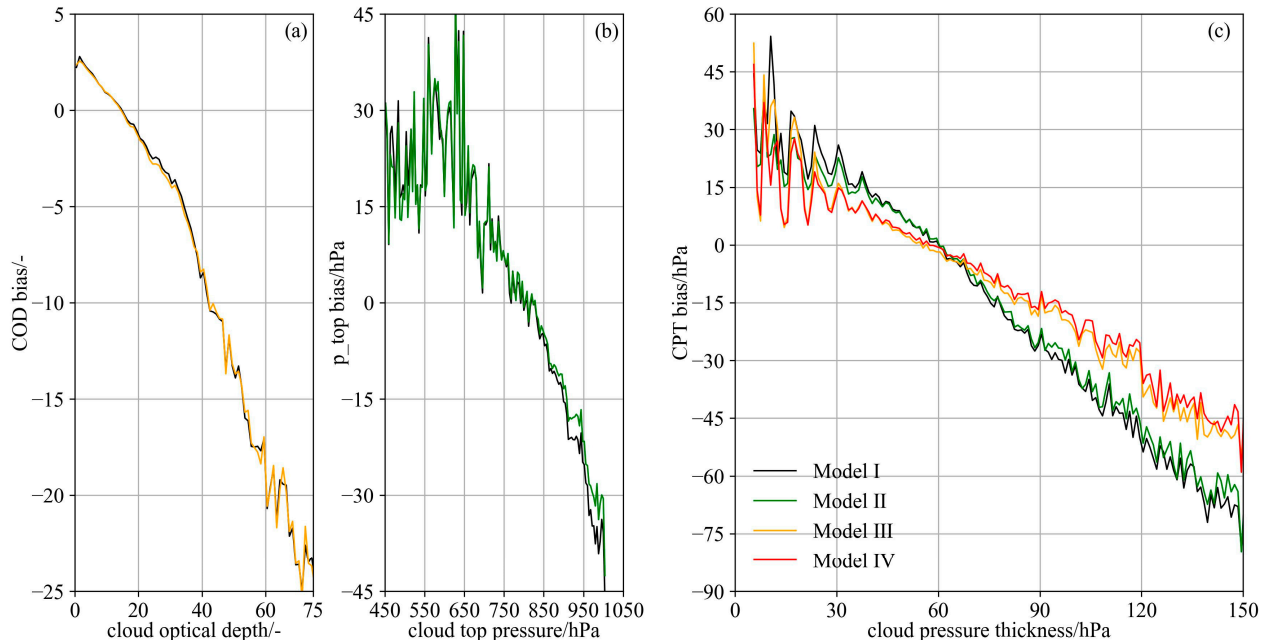
In Model IV, both the COD and  $p_{top}$  are input variables, and the RMSE of the CPT is the smallest among the four experiments. The estimation of geometrically thin clouds (CPT < 15 hPa) is influenced by the vertical resolution of the CALIOP and may not have enough samples (10 of 15 bins have less than 50 samples) to obtain confident RMSEs. Furthermore, all the models perform best for CPT ranging from 50 hPa to 70 hPa, with a similar RMSE < 20 hPa, showing that sufficient samples can improve the prediction accuracy to a certain degree.

Figure 6 compares the effects of known CODs and  $p_{top}$ s on the bias of other CVS parameters in the four experiments. The additional  $p_{top}$  in Figure 6a does not weaken the bias of the COD, nor does the additional COD in Figure 6b, suggesting, again, that the COD and  $p_{top}$  are two relatively independent variables. In Figure 6c, the  $p_{top}$  input can reduce the CPT prediction bias notably for all scenes. CPT predictions have biases larger than 30 hPa for CPTs < 10 hPa in Model I, while the bias of the predicted CPT decreases notably with the known  $p_{top}$ s in Models III and IV. Attributed to the limitation of information content in OCO-2 hyperspectral oxygen A-band measurements, few data (about 1%) distributed in CPTs < 10 hPa are overestimated by the NN model in the prediction, and more information content used as input can significantly decrease the biases. The comparison suggests that the information content in the OCO-2 hyperspectral oxygen A-band is still limited for CPT prediction. Our study is a supplement to CPT retrieval based on the oxygen A-band.

#### 4.2.3. Analysis over Land and Ocean Surfaces

In the previous optimal estimation-based CPT retrievals based on OCO-2 oxygen A-band observations by Richardson et al. and Yang et al. [26,31], clouds over land surfaces are not discussed because of the complexity of the land surfaces and difficulties in the acquisition of the accurate surface albedo, whose uncertainties may influence the prediction. Both land and marine clouds are included in the test dataset, with 376,236 samples over the ocean and 91,078 samples over the land. The comparison of the prediction results of the

two types of clouds can analyze the influence of the surface type on the prediction. The comparison is only for clouds with a CPT > 15 hPa to avoid unreliable conclusions, as only 272 land samples are collected when the CPT < 15 hPa, and 11 of 15 bins of marine clouds contain less than 50 samples.



**Figure 6.** Biases of (a) COD, (b)  $p_{top}$ , and (c) CPT in the predictions of Model I–IV.

Figure 7 compares the RMSE of Model I and III over the ocean and land. In both Model I and III, the RMSEs of marine clouds are worse than those of land clouds when the CPT < 70 hPa, and the RMSEs of marine clouds are better than those of land clouds when the CPT > 70 hPa. After adding the  $p_{top}$  as input, the RMSE of both land and marine clouds decreases, but the accuracy of marine clouds improves more significantly when the CPT > 70 hPa, indicating that known  $p_{top}$ s is more helpful for CPT prediction of marine clouds than land clouds.

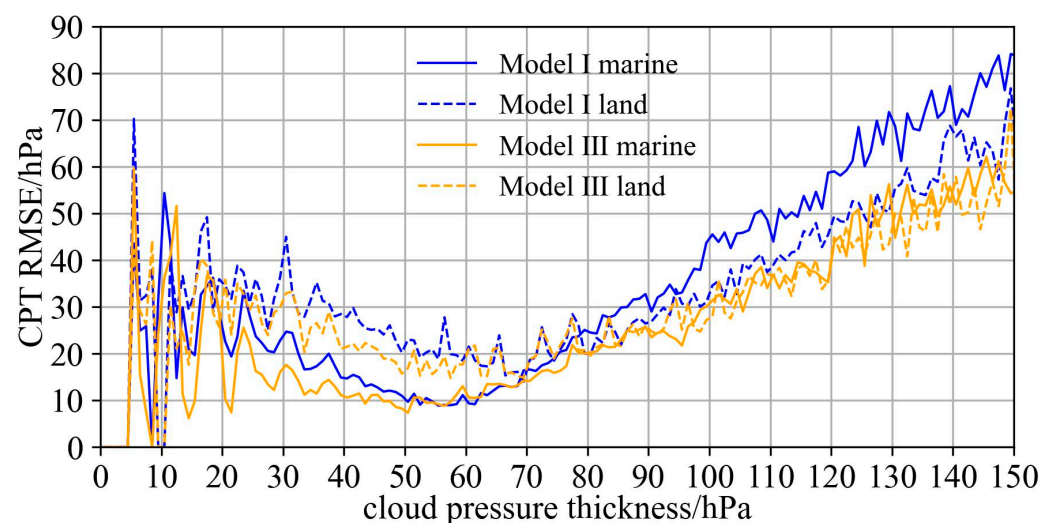


**Figure 7.** RMSE of predicted CPT prediction with and without known  $p_{top}$  inputs above the surface and land surfaces. The blue line represents prediction without collocated input (Model I), while the orange line represents the prediction with  $p_{top}$  input (Model III). The solid line represents the results over the ocean surface, while the dashed line represents results over the land surface.



Figure 9a–c compare the RMSEs of the OCO2CLD-LIDAR-AUX product, Model I, and Model III. With respect to the collocated OCO2CLD-LIDAR-AUX product, Model I has a better RMSE of the COD for CODs > 5, a better RMSE of the  $p_{top}$  for  $650 \text{ hPa} < p_{tops} < 900 \text{ hPa}$ , and a much better RMSE of the CPT for CPTs > 30 hPa. Model III has a comparable RMSE of the CPT for CPTs < 30 hPa and a much better RMSE for CPTs > 30 hPa. Figure 9d shows the bias of the OCO2CLD-LIDAR-AUX product and Model I. The predicted CPT in Model I has a higher overestimation than the OCO2CLD-LIDAR-AUX when the CPT < 30 hPa, while Model I has a much lower underestimation when the CPT > 60 hPa, and the CPTs in Model III have a better bias than Model I for CPTs < 30 hPa.

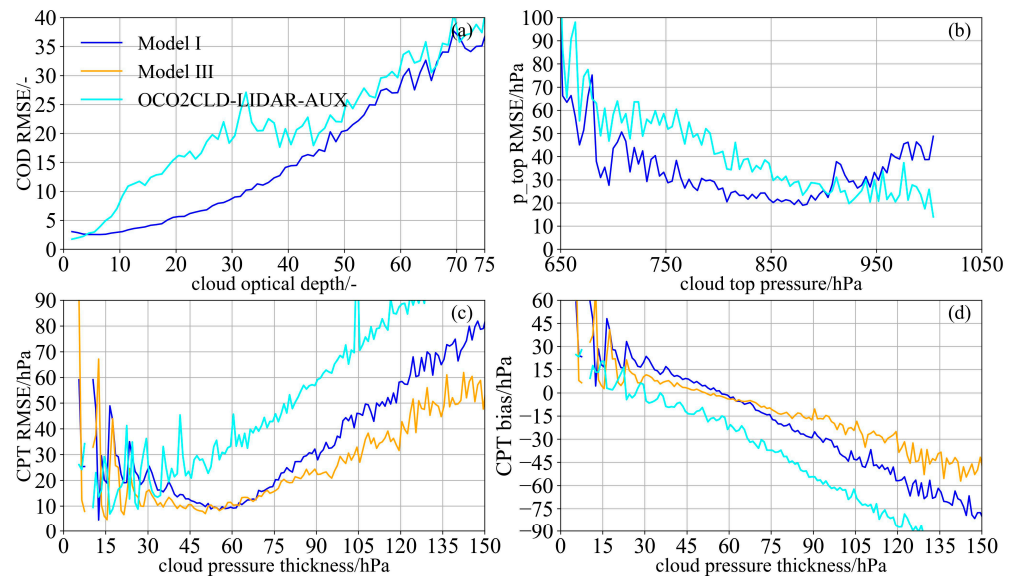


**Figure 9.** RMSE and bias of Model I, Model III, and the OCO2CLD-LIDAR-AUX compared with the collocated dataset. (a–c) display the RMSE of (a) COD versus MYD06\_L2, bin size = 1, (b)  $p_{top}$  versus 2B-CLDCLASS-LIDAR, bin size = 6 hPa, and (c) CPT versus OCO2CLD-LIDAR-AUX, bin size = 1 hPa. (d) displays the bias versus CPT with the same bin size as in (c).

In summary, compared with the OCO2CLD-LIDAR-AUX, our algorithm has better CODs for all clouds, better  $p_{tops}$  for clouds whose  $p_{top} < 900 \text{ hPa}$ , and better CPT for clouds whose CPT > 30 hPa. Additional known  $p_{tops}$  can further improve the performance of our algorithm.

## 5. Conclusions

In this paper, we developed a cloud vertical structure (CVS) prediction algorithm based on a neural network only using OCO-2 oxygen A-band measurements for single-layer liquid clouds. Our algorithm can predict three parameters, including the cloud optical depth (COD), cloud top pressure ( $p_{top}$ ), and cloud pressure thickness (CPT), at the same time without collocated  $p_{top}$  input, getting rid of the lack of collocated  $p_{tops}$  caused by the exit of CALIPSO and CloudSat. The correlation coefficients of the COD,  $p_{top}$ , and CPT are 0.8178 (versus the MYD06\_L2), 0.9514 and 0.5280 (versus the 2B-CLDCLASS-LIDAR), and the RMSEs are 7.31, 35.06 hPa, and 26.66 hPa.

Known COD and  $p_{top}$  inputs influence the CPT. Collocated COD and  $p_{top}$  inputs can improve the accuracy of the CPT, with the R of the CPT increasing to 0.7449 and the RMSE decreasing to 20.82 hPa. The CPT reaches a much better accuracy than the previous algorithm [31] with the same collocated COD and  $p_{top}$  inputs (38.5 hPa). The impact of the COD and  $p_{top}$  on CPT prediction varies with the clouds' properties. Collocated CODs can reduce the RMSE of geometrically thin clouds in the CPT, when the  $p_{top}$  plays a more significant role, greatly reducing the RMSE and bias in the CPT.

Differences in the CPT prediction between land and marine surfaces are assessed. Marine surfaces show a higher accuracy for thin clouds, and land surfaces show a higher accuracy for thick clouds. With a collocated  $p_{top}$  constraint, the error of both land and marine clouds is reduced, and marine clouds still have a higher accuracy for geometrically thin clouds and a similar accuracy for thick clouds.

The prediction results were compared with the OCO2CLD-LIDAR-AUX product, a CVS product retrieved based on the same oxygen A-band measurements, to compare our statistical algorithm with the physical retrieval method. Compared with the OCO2CLD-LIDAR-AUX (versus the MYD06\_L2 and 2B-CLDCLASS-LIDAR), our algorithm provides better CODs for all clouds, better  $p_{tops}$  for clouds with a top pressure less than 900 hPa, and better CPTs for clouds thicker than 30 hPa. Our algorithm has higher accuracy (RMSE: 26.66 hPa < 35.39 hPa) in the CPT without vital collocated  $p_{top}$  input.

This study is an improvement on CVS prediction based on the OCO-2 after the exit of CloudSat and CALIPSO. This algorithm provides a meaningful method for CVS prediction without known collocated  $p_{tops}$  and provides the possibility for high accuracy CVS prediction based on passive sensors. Further research can add collocated passive remote sensing measurements, such as brightness temperature MODIS observation, to provide  $p_{top}$  information for CPT prediction. However, this algorithm cannot select single-layer liquid clouds from OCO-2 measurements. Algorithms for detection of cloud layers and the thermodynamic phase based on passive observation are needed for preprocessing in this algorithm. Furthermore, our algorithm needs further improvement to predict the CVS of multi-layer clouds (Figure S3).

**Supplementary Materials:** The following supporting information can be downloaded at: <https://www.mdpi.com/article/10.3390/rs15123142/s1>, Table S1: Models in the sample-based cross-validation and their prediction accuracy. Figure S1: Prediction result based on the single-layer liquid clouds with above-cloud aerosols. Figure S2: A view of predicted CVS of Model I along OCO-2 track. Figure S3: Prediction result based on the multi-layer clouds with  $p_{top} > 650$  hPa.

**Author Contributions:** Y.L. and J.Y. conceived the paper and developed the algorithm; Y.L. wrote the manuscript and prepared the figures and tables; Y.L. and J.Y. contributed to the data processing and analysis; S.L. and J.Y. supervised the preparation of the manuscript. All authors have read and agreed to the published version of the manuscript.

**Funding:** This research was funded by the National Natural Science Foundation of China (No. 42205129 and 41975022), the Fundamental Research Funds for Central Universities (No. 2042022kf1064), and the China Postdoctoral Science Foundation (No. 2022M712445).

**Data Availability Statement:** 2B-CLDCLASS-LIDAR data for this study are available at (<https://www.cloudsat.cira.colostate.edu/data-products/2b-cldclass-lidar>, accessed on 13 May 2023). 2B-CLDCLASS data for this study are available at (<https://www.cloudsat.cira.colostate.edu/data-products/2b-cldclass>, accessed on 13 May 2023). CAL\_LID\_L2\_05kmALay data for this study are available at ([https://asdc.larc.nasa.gov/project/CALIPSO/CAL\\_LID\\_L2\\_05kmALay-Standard-V4-20\\_V4-20](https://asdc.larc.nasa.gov/project/CALIPSO/CAL_LID_L2_05kmALay-Standard-V4-20_V4-20), accessed on 13 May 2023). MODIS data for this study are available at ([https://ladsweb.modaps.eosdis.nasa.gov/archive/allData/61/MYD06\\_L2/](https://ladsweb.modaps.eosdis.nasa.gov/archive/allData/61/MYD06_L2/), accessed on 13 May 2023). OCO-2 data (version 8r) for this study are no longer available on NASA's official website, but Version 10r is available at ([https://search.earthdata.nasa.gov/search/granules?p=C1685783889-GES\\_DISC&pg\[0\]\[v\]=f&tl=1683808995!3!!](https://search.earthdata.nasa.gov/search/granules?p=C1685783889-GES_DISC&pg[0][v]=f&tl=1683808995!3!!), accessed on 13 May 2023). OCO2CLD-LIDAR-AUX data are available at (<https://www.cloudsat.cira.colostate.edu/data-products/oco2cld-lidar-aux>, accessed on 13 May 2023).

**Acknowledgments:** The authors are thankful for the advice from professional reviewers and the assistance of the editorial team of Remote Sensing.

**Conflicts of Interest:** The authors declare no conflict of interest.

## References

1. Rossow, W.B.; Schiffer, R.A. Advances in understanding clouds from ISCCP. *Bull. Am. Meteorol. Soc.* **1999**, *80*, 2261–2288. [[CrossRef](#)]
2. Stephens, G.L. Cloud feedbacks in the climate system: A critical review. *J. Clim.* **2005**, *18*, 237–273. [[CrossRef](#)]

3. Yang, Q.; Fu, Q.; Hu, Y. Radiative impacts of clouds in the tropical tropopause layer. *J. Geophys. Res. Atmos.* **2010**, *115*, D00H12. [[CrossRef](#)]
4. Stevens, B.; Bony, S. What are climate models missing? *Science* **2013**, *340*, 1053–1054. [[CrossRef](#)] [[PubMed](#)]
5. George, G.; Sarangi, C.; Tripathi, S.N.; Chakraborty, T.; Turner, A. Vertical structure and radiative forcing of monsoon clouds over Kanpur during the 2016 INCOMPASS field campaign. *J. Geophys. Res. Atmos.* **2018**, *123*, 2152–2174. [[CrossRef](#)]
6. Ravi Kiran, V.; Rajeevan, M.; Gadhavi, H.; Rao, S.V.B.; Jayaraman, A. Role of vertical structure of cloud microphysical properties on cloud radiative forcing over the Asian monsoon region. *Clim. Dyn.* **2015**, *45*, 3331–3345. [[CrossRef](#)]
7. Li, J.; Yi, Y.; Minnis, P.; Huang, J.; Yan, H.; Ma, Y.; Wang, W.; Ayers, J.K. Radiative effect differences between multi-layered and single-layer clouds derived from CERES, CALIPSO, and CloudSat data. *J. Quant. Spectrosc. Radiat. Transf.* **2011**, *112*, 361–375. [[CrossRef](#)]
8. Narendra Reddy, N.; Venkat Ratnam, M.; Basha, G.; Ravikiran, V. Cloud vertical structure over a tropical station obtained using long-term high-resolution radiosonde measurements. *Atmos. Chem. Phys.* **2018**, *18*, 11709–11727. [[CrossRef](#)]
9. Jakob, C.; Klein, S.A. The role of vertically varying cloud fraction in the parametrization of microphysical processes in the ECMWF model. *Q. J. R. Meteorol. Soc.* **1999**, *125*, 941–965. [[CrossRef](#)]
10. Yan, Y.; Liu, Y.; Lu, J. Cloud vertical structure, precipitation, and cloud radiative effects over Tibetan Plateau and its neighboring regions. *J. Geophys. Res. Atmos.* **2016**, *121*, 5864–5877. [[CrossRef](#)]
11. Wang, J.; Rossow, W.B. Effects of cloud vertical structure on atmospheric circulation in the GISS GCM. *J. Clim.* **1998**, *11*, 3010–3029. [[CrossRef](#)]
12. Weare, B.C. Insights into the importance of cloud vertical structure in climate. *Geophys. Res. Lett.* **2000**, *27*, 907–910. [[CrossRef](#)]
13. Stephens, G.L.; Vane, D.G.; Boain, R.J.; Mace, G.G.; Sassen, K.; Wang, Z.; Illingworth, A.J.; O’connor, E.J.; Rossow, W.B.; Durden, S.L. The CloudSat mission and the A-Train: A new dimension of space-based observations of clouds and precipitation. *Bull. Am. Meteorol. Soc.* **2002**, *83*, 1771–1790. [[CrossRef](#)]
14. Winker, D.M.; Hunt, W.H.; McGill, M.J. Initial performance assessment of CALIOP. *Geophys. Res. Lett.* **2007**, *34*, L19803. [[CrossRef](#)]
15. Oreopoulos, L.; Cho, N.; Lee, D. New insights about cloud vertical structure from CloudSat and CALIPSO observations. *J. Geophys. Res. Atmos.* **2017**, *122*, 9280–9300. [[CrossRef](#)] [[PubMed](#)]
16. Hanel, R.A. Determination of cloud altitude from a satellite. *J. Geophys. Res.* **1961**, *66*, 4. [[CrossRef](#)]
17. Yamamoto, G.; Wark, D. Discussion of the letter by RA Hanel, “Determination of cloud altitude from a satellite”. *J. Geophys. Res.* **1961**, *66*, 3596. [[CrossRef](#)]
18. Drouin, B.J.; Benner, D.C.; Brown, L.R.; Cich, M.J.; Crawford, T.J.; Devi, V.M.; Guillaume, A.; Hodges, J.T.; Mlawer, E.J.; Robichaud, D.J. Multispectrum analysis of the oxygen A-band. *J. Quant. Spectrosc. Radiat. Transf.* **2017**, *186*, 118–138. [[CrossRef](#)]
19. Rozanov, V.V.; Kokhanovsky, A.A. Semianalytical cloud retrieval algorithm as applied to the cloud top altitude and the cloud geometrical thickness determination from top-of-atmosphere reflectance measurements in the oxygen A band. *J. Geophys. Res. Atmos.* **2004**, *109*, D05202. [[CrossRef](#)]
20. Schuessler, O.; Rodriguez, D.G.L.; Doicu, A.; Spurr, R. Information Content in the Oxygen A-Band for the Retrieval of Macrophysical Cloud Parameters. *IEEE Trans. Geosci. Remote Sens.* **2013**, *52*, 3246–3255. [[CrossRef](#)]
21. Kokhanovsky, A.A.; Rozanov, V.V. Cloud bottom altitude determination from a satellite. *IEEE Geosci. Remote Sens. Lett.* **2005**, *2*, 280–283. [[CrossRef](#)]
22. Rozanov, V.V.; Kokhanovsky, A.A. Determination of cloud geometrical thickness using backscattered solar light in a gaseous absorption band. *IEEE Geosci. Remote Sens. Lett.* **2006**, *3*, 250–253. [[CrossRef](#)]
23. Ferlay, N.; Thieuleux, F.; Cornet, C.; Davis, A.B.; Dubuisson, P.; Ducos, F.; Parol, F.; Riédi, J.; Vanbauce, C. Toward new inferences about cloud structures from multidirectional measurements in the oxygen A band: Middle-of-cloud pressure and cloud geometrical thickness from POLDER-3/PARASOL. *J. Appl. Meteorol. Climatol.* **2010**, *49*, 2492–2507. [[CrossRef](#)]
24. Merlin, G.; Riédi, J.; Labonnote, L.C.; Cornet, C.; Davis, A.B.; Dubuisson, P.; Desmons, M.; Ferlay, N.; Parol, F. Cloud information content analysis of multi-angular measurements in the oxygen A-band: Application to 3MI and MSPI. *Atmos. Meas. Tech.* **2016**, *9*, 4977–4995. [[CrossRef](#)]
25. Yang, Y.; Marshak, A.; Mao, J.; Lyapustin, A.; Herman, J. A method of retrieving cloud top height and cloud geometrical thickness with oxygen A and B bands for the Deep Space Climate Observatory (DSCOVR) mission: Radiative transfer simulations. *J. Quant. Spectrosc. Radiat. Transf.* **2013**, *122*, 141–149. [[CrossRef](#)]
26. Richardson, M.; Leinonen, J.; Cronk, H.Q.; McDuffie, J.; Lebsock, M.D.; Stephens, G.L. Marine liquid cloud geometric thickness retrieved from OCO-2’s oxygen A-band spectrometer. *Atmos. Meas. Tech.* **2019**, *12*, 1717–1737. [[CrossRef](#)]
27. Fischer, J.; Grassl, H. Detection of cloud-top height from backscattered radiances within the oxygen A band. Part 1: Theoretical study. *J. Appl. Meteorol. Climatol.* **1991**, *30*, 1245–1259. [[CrossRef](#)]
28. Koelemeijer, R.; Stammes, P.; Hovenier, J.; De Haan, J. A fast method for retrieval of cloud parameters using oxygen A band measurements from the Global Ozone Monitoring Experiment. *J. Geophys. Res. Atmos.* **2001**, *106*, 3475–3490. [[CrossRef](#)]
29. Stephens, G.L.; Heidinger, A. Molecular line absorption in a scattering atmosphere. Part I: Theory. *J. Atmos. Sci.* **2000**, *57*, 1599–1614. [[CrossRef](#)]
30. Richardson, M.; Stephens, G.L. Information content of OCO-2 oxygen A-band channels for retrieving marine liquid cloud properties. *Atmos. Meas. Tech.* **2018**, *11*, 1515–1528. [[CrossRef](#)]

31. Yang, J.; Li, S.; Gong, W.; Min, Q.; Mao, F.; Pan, Z. A fast cloud geometrical thickness retrieval algorithm for single-layer marine liquid clouds using OCO-2 oxygen A-band measurements. *Remote Sens. Environ.* **2021**, *256*, 112305. [[CrossRef](#)]
32. Sun, K.; Liu, X.; Nowlan, C.R.; Cai, Z.; Chance, K.; Frankenberg, C.; Lee, R.A.; Pollock, R.; Rosenberg, R.; Crisp, D. Characterization of the OCO-2 instrument line shape functions using on-orbit solar measurements. *Atmos. Meas. Tech.* **2017**, *10*, 939–953. [[CrossRef](#)]
33. Lee, R.A.; O'Dell, C.W.; Wunch, D.; Roehl, C.M.; Osterman, G.B.; Blavier, J.-F.; Rosenberg, R.; Chapsky, L.; Frankenberg, C.; Hunyadi-Lay, S.L. Preflight spectral calibration of the Orbiting Carbon Observatory 2. *IEEE Trans. Geosci. Remote Sens.* **2017**, *55*, 2499–2508. [[CrossRef](#)]
34. Crisp, D. Measuring atmospheric carbon dioxide from space with the Orbiting Carbon Observatory-2 (OCO-2). *Proc. Earth Obs. Syst.* **2015**, *9607*, 960702.
35. Wunch, D.; Wennberg, P.O.; Osterman, G.; Fisher, B.; Naylor, B.; Roehl, C.M.; O'Dell, C.; Mandrake, L.; Viatte, C.; Kiel, M. Comparisons of the orbiting carbon observatory-2 (OCO-2) X CO<sub>2</sub> measurements with TCCON. *Atmos. Meas. Tech.* **2017**, *10*, 2209–2238. [[CrossRef](#)]
36. Eldering, A.; O'Dell, C.W.; Wennberg, P.O.; Crisp, D.; Gunson, M.R.; Viatte, C.; Avis, C.; Braverman, A.; Castano, R.; Chang, A. The Orbiting Carbon Observatory-2: First 18 months of science data products. *Atmos. Meas. Tech.* **2017**, *10*, 549–563. [[CrossRef](#)]
37. Massie, S.T.; Sebastian Schmidt, K.; Eldering, A.; Crisp, D. Observational evidence of 3-D cloud effects in OCO-2 CO<sub>2</sub> retrievals. *J. Geophys. Res. Atmos.* **2017**, *122*, 7064–7085. [[CrossRef](#)]
38. Boesch, H.; Brown, L.; Castano, R.; Christi, M.; Connor, B.; Crisp, D.; Eldering, A.; Fisher, B.; Frankenberg, C.; Gunson, M. *Orbiting Carbon Observatory (OCO)-2 Level 2 Full Physics Retrieval Algorithm Theoretical Basis Document*; NASA JPL: Pasadena, CA, USA, 2015.
39. Sassen, K.; Wang, Z.; Liu, D. Global distribution of cirrus clouds from CloudSat/Cloud-Aerosol lidar and infrared pathfinder satellite observations (CALIPSO) measurements. *J. Geophys. Res. Atmos.* **2008**, *113*, D00A12. [[CrossRef](#)]
40. Sassen, K.; Wang, Z. Classifying clouds around the globe with the CloudSat radar: 1-year of results. *Geophys. Res. Lett.* **2008**, *35*, L04805. [[CrossRef](#)]
41. Marchant, B.; Platnick, S.; Meyer, K.; Arnold, G.T.; Riedi, J. MODIS Collection 6 shortwave-derived cloud phase classification algorithm and comparisons with CALIOP. *Atmos. Meas. Tech.* **2016**, *9*, 1587–1599. [[CrossRef](#)]
42. Platnick, S.; Meyer, K.G.; King, M.D.; Wind, G.; Amarasinghe, N.; Marchant, B.; Arnold, G.T.; Zhang, Z.; Hubanks, P.A.; Holz, R.E. The MODIS cloud optical and microphysical products: Collection 6 updates and examples from Terra and Aqua. *IEEE Trans. Geosci. Remote Sens.* **2016**, *55*, 502–525. [[CrossRef](#)]
43. Taylor, T.E.; O'Dell, C.W.; Frankenberg, C.; Partain, P.T.; Cronk, H.Q.; Savtchenko, A.; Nelson, R.R.; Rosenthal, E.J.; Chang, A.Y.; Fisher, B. Orbiting Carbon Observatory-2 (OCO-2) cloud screening algorithms: Validation against collocated MODIS and CALIOP data. *Atmos. Meas. Tech.* **2016**, *9*, 973–989. [[CrossRef](#)]
44. Saponaro, G.; Kolmonen, P.; Karhunen, J.; Tamminen, J.; de Leeuw, G. A neural network algorithm for cloud fraction estimation using NASA-Aura OMI VIS radiance measurements. *Atmos. Meas. Tech.* **2013**, *6*, 2301–2309. [[CrossRef](#)]
45. Yu, W.; Xu, X.; Jin, S.; Ma, Y.; Liu, B.; Gong, W. BP neural network retrieval for remote sensing atmospheric profile of ground-based microwave radiometer. *IEEE Geosci. Remote Sens. Lett.* **2021**, *19*, 4502105. [[CrossRef](#)]
46. Rodriguez, D.G.L.; Thomas, W.; Livschitz, Y.; Ruppert, T.; Albert, P.; Hollmann, R. Cloud properties derived from GOME/ERS-2 backscatter data for trace gas retrieval. *IEEE Trans. Geosci. Remote Sens.* **2007**, *45*, 2747–2758. [[CrossRef](#)]
47. Loyola, D.; Koukoulis, M.; Valks, P.; Balis, D.; Hao, N.; Van Roozendaal, M.; Spurr, R.; Zimmer, W.; Kiemle, S.; Lerot, C. The GOME-2 total column ozone product: Retrieval algorithm and ground-based validation. *J. Geophys. Res. Atmos.* **2011**, *116*, D07302. [[CrossRef](#)]
48. Loyola, D.G.; Gimeno García, S.; Lutz, R.; Argyrouli, A.; Romahn, F.; Spurr, R.J.; Pedernana, M.; Doicu, A.; Molina García, V.; Schüssler, O. The operational cloud retrieval algorithms from TROPOMI on board Sentinel-5 Precursor. *Atmos. Meas. Tech.* **2018**, *11*, 409–427. [[CrossRef](#)]

**Disclaimer/Publisher's Note:** The statements, opinions and data contained in all publications are solely those of the individual author(s) and contributor(s) and not of MDPI and/or the editor(s). MDPI and/or the editor(s) disclaim responsibility for any injury to people or property resulting from any ideas, methods, instructions or products referred to in the content.